Microstructure and Microhardness of High-Strength Aluminium Alloy Prepared Using High-Speed Laser Fabrication

Yu Wu [1], Bingqing Chen [1,*], Peixin Xu [2], Pengjun Tang [3], Borui Du [2] and Chen Huang [4]

1   3D Printing Research & Engineering Technology Center, Beijing Institute of Aeronautical Materials, Beijing 100095, China
2   China Machinery Institute of Advanced Materials (Zhengzhou) Co., Ltd., Zhengzhou 450001, China
3   Institute of Aluminium Alloy, Beijing Institute of Aeronautical Materials, Beijing 100095, China
4   Petrochemical Department, China National Petroleum & Chemical Planning Institute, Beijing 100013, China
*   Correspondence: hwtkjcbq1984@163.com

Abstract: As a recently developed high-strength aluminium alloy used specifically for laser additive manufacturing, AlMgMnSc alloy possesses superior mechanical properties and excellent processability. Extreme high-speed laser deposition (EHLD) is a novel surface-modification technique, which is characterised by high depositing speed, rapid cooling, rate and minimal dilution rate. To offer a new method for surface repairing high-strength aluminium alloys, an AlMgMnSc alloy coating, containing two deposition layers, is prepared on a 6061 aluminium-alloy axle using the EHLD technique. Meanwhile, the microstructure, composition distribution, and microhardness variation of the fabricated coating are studied. The results reveal that the coating is dense and crack-free, which is well-bonded with the substrate. Additionally, layer 1 is mainly composed of large columnar and equiaxed grains, while layer 2 consists of a fully equiaxed grain structure with an average grain size of about 4.5 μm. Moreover, the microhardness of the coating (about 104~118 HV) is similar to the substrate (about 105 HV), proving the feasibility of repairing high-strength aluminium alloys using AlMgMnSc alloy powders through the EHLD technique.

Keywords: microstructure; microhardness; composition; grain structure; high-strength aluminium alloy; extreme high-speed laser deposition

1. Introduction

Extreme high-speed laser deposition (EHLD) is a novel material-surface-modification technique, which was developed by Fraunhofer Laser Technology Research Institute in 2013 [1,2]. In conventional laser deposition, primary energy is deposited into the substrate instead of into powders. As for the EHLD, most of the laser energy is absorbed by powders, decreasing the heat input to the substrate remarkably [3]. During the EHLD process, raw materials are fed by a coaxial powder feed nozzle, with the focus of the powder flow above the substrate. Most of the laser energy is absorbed by the powders before they reach the substrate; only a small melting pool is formed on the substrate surface by residual laser energy. As a result, powder particles are melted by the laser beam before hitting the substrate, entering the melting pool in a molten or semi-molten state [4,5]. Consequently, the EHLD has the advantages of high depositing speed, rapid cooling rate, and minimal dilution rate, providing high economic benefits and satisfactory material performance [2,6]. As is reported, the processing speed and deposition efficiency of the EHLD can be up to 500 m/min and 96%, respectively [7].

Currently, the EHLD is mainly used to modify the surfaces of Ni-based alloy, Fe-based based alloy, amorphous alloys, high-entropy alloys, and metal matrix composite coatings [6,8–16]. Yuan et al. [1] deposited Ni45 alloy coatings on 45 medium carbon steel substrates by a traditional laser-deposition technique and the EHLD, respectively. It is reported that the coating fabricated using the EHLD has a lower roughness and a smaller

thickness when compared with the traditional laser-deposition technique. Meanwhile, variations in processing parameters lead to changes in the solidification conditions of the melting pool. A fine equiaxial dendritic structure could be obtained under a high laser cladding rate. Zhang et al. [4] established a powder flow model by using a transient bidirectional coupling calculation method to investigate the effects of laser power, carrier-gas flow rate, and shielding-gas flow rate on particle temperature profiles during the EHLD process. According to their results, the carrier-gas and protective-gas flow rates are key factors for determining the maximum elevation angle of the powder flow. With the increase in carrier-gas flow, there is an increase in the maximum inclination angle of the powder. On the other hand, the increase in shielding-gas flow could lead to a decrease in the maximum inclination angle of the powder. Koß et al. [7] investigated the maximum surface rate and deposition rate by depositing an AlSi10Mg coating on an AlMgSi0.5 alloy substrate using the EHLD with a conventional 8 kW IR-laser beam source. The results demonstrate the feasibility of fabricating an aluminium coating on an aluminium-alloy substrate through the EHLA. At a processing speed of 100 m/min, a maximum surface rate of 800 cm^2/min and deposition rate of about 22.5 g/min could be obtained. Meanwhile, a maximum surface rate of 1300 cm^2/min and a deposition rate of about 34 g/min were achieved at a processing speed of 200 m/min. It is proposed that it is possible to increase the surface and deposition rate by increasing the laser power using the EHLD.

High-strength aluminium alloys are used in a broad range of industries, such as the automobile, aerospace, and construction industries and mechanical and electrical engineering [17–19]. The world's top-three largest consumers of primary aluminium are China (33.3 million tons), the USA (4.6 million tons), and Germany (2.1 million tons) [7]. As is reported, aluminium alloys make up 60–80% of the weight of a commercial aircraft and more than 50% of the structural quality of rockets and aircraft [20,21]. The 6xxx series alloy is a kind of high-strength aluminium alloy. It is reported that the application proportion of the 6xxx series alloy in civil aircraft is about 6% [20]. A typical 6xxx series alloy is 6061 aluminium alloy, which is a heat-treated, precipitation hardened, alloy and includes magnesium (Mg), silicon (Si), and iron (Fe) as its major alloying elements [22]. The 6061 aluminium alloy offers low density, high strength-to-weight ratio, good ductility, excellent formability and weldability, good corrosion resistance, and low cost [22]. Currently, it is mainly adopted to fabricate aircraft wings, fuselages, and fuel tanks and in wheel rims, wheel spacers, truck bodies, car frames, bicycle frames, bike frames, container bodies, goods wagons, carriages, trams, driveshafts, valves, etc. [22,23].

The long-term performance of high-strength aluminium-alloy components under certain conditions is limited due to their high coefficient of friction, poor wear characteristics, and low hardness. Additionally, it is reported that about 423.2 kWh of electricity and about 558 Nm^3 of natural gas are needed to produce 1 t of primary aluminium, while recycling requires only about 5% of the energy [7]. Consequently, surface repair and modification are of great importance for high-strength aluminium alloys to reduce material quantity and manufacturing costs.

As is known, the preparation of traditional high-strength aluminium alloys through laser processing is challenging because they normally present high susceptibility to cracking due to large liquidus-to-solidus temperature ranges and high solidification rates during fabrication [24–28]. Tan et al. [25] analysed the influence of processing parameters on the cracking of a 2024 aluminium alloy prepared by laser processing. It is suggested that a reduction in the fraction of large elongated columnar grains could lead to a decrease in hot cracks. However, it is impossible to eliminate columnar grains by adjusting processing parameters. Thus, hot cracks in laser-processed 2024 aluminium alloys could hardly be completely avoided. Wojciech et al. [26] optimised the processing parameters of a 7075 aluminium alloy fabricated through laser processing. Their results indicate that solidification cracks along columnar grain boundaries could hardly be totally eliminated. Furthermore, intergranular micro-segregation of Zn, Mg, Cu, and Si are observed. It is considered that Si may result in a high cracking susceptibility by increasing the stability

of the liquid film. Yao et al. [28] studied the formation mechanism of cracks in a laser-processed 2024 aluminium alloy. They proposed that the transverse strain rate of columnar grains could easily exceed the sum of the transverse expansion rate of grains and the filling rate of liquids at the grain boundaries due to high Cu and Mg contents. In addition, the high cooling rate and heat input involved in laser processing reduce the filling rate of liquids at grain boundaries. As a result, a 2024 aluminium alloy presents strong thermal crack sensitivity during laser processing. Therefore, the application of laser processing in surface repair and modification of high-strength aluminium alloys is significantly limited.

Very recently, Sc-containing high-strength aluminium alloys have been designed specifically for laser additive manufacturing (LAM) [24,29–36]. In LAMed AlMgMnSc alloys, primary Al_3Sc particles would precipitate in the melting pool before solidification of the α-Al, providing heterogeneous nucleation sites for α-Al grains [30]. As a result, the formation of equiaxed fine grains is promoted, which mitigates solidification cracking significantly. Meanwhile, the addition of Sc remarkably improves the mechanical properties of aluminium alloys. Wang et al. [31] studied the influence of solidification conditions on the microstructure and mechanical property of an aluminium alloy fabricated through laser-directed energy deposition. It was found that an equiaxed grain structure could be obtained at a low cooling rate, while a heterogeneous grain structure containing a fine grain band and a fan-shaped coarse grain was formed at a high cooling rate. After ageing, the yield strength of the sample prepared at a high cooling rate is enhanced to ~2 times that of the sample prepared at a low cooling rate. Hua et al. [32] prepared aluminium alloys with a fully equiaxed grain structure with grain sizes of 2–30 μm through laser-directed energy deposition. Most of the primary Al_3Sc particles were found along grain boundaries. The deposited alloy presents a certain but not obvious anisotropy, since the texture index and strength are only slightly larger than 1. Yield strength, tensile strength, and elongation of the specimen in the horizontal direction and the building direction are 399.87 MPa, 220.96 MPa, 9.13% and 385.40 MPa, 219.40 MPa, 8.24%, respectively.

Although the successful preparation of AlMgMnSc alloys through LAM suggests that it could be possible to modify the surfaces of aluminium alloys through the EHLD technique, research in this field is seldom conducted. The microstructure characteristics and mechanical behaviour of the EHLDed AlMgMnSc alloy coating remain unclear. Therefore, the EHLD approach was used in this work to fabricate an AlMgMnSc alloy coating on a 6061 aluminium-alloy axle. Additionally, the microstructure, composition, distribution, and microhardness variation of the prepared coating were analysed. Meanwhile, the microstructure formation mechanism of the deposited coating was investigated. The aim of this paper is to offer a comprehensive understanding of the microstructure and mechanical property of the EHLDed AlMgMnSc alloy coating, providing theoretical guidance for surface repairing of a high-strength aluminium alloy using the EHLD technique.

2. Materials and Methods

An annealed wrought 6061 aluminium-alloy axle with a diameter of 60 mm was applied as a substrate. The composition and microhardness of the substrate are about Al-1.12Mg-0.18Cu-0.12Mn-0.17Zn-0.19Cr-0.06Ti-0.61Si-0.55Fe (wt.%) and 105 HV, respectively. Spherical AlMgMnSc alloy powders with particle sizes ranging from 15 to 53 μm were adopted as feedstock material (D_{10}: 17.30 μm, D_{50}: 33.15 μm, and D_{90}: 55.58 μm). The apparent density and tap density of the powders are 1.40 g/cm^3 and 1.7 g/cm^3, respectively. Figure 1 illustrates the SEM images of the powders. As shown in Figure 1a, the powders have a spherical shape. It is also noticed that some planetary powders are distributed on the surfaces of powders (see Figure 1b). The nominal composition of the AlMgMnSc alloy is Al-5Mg-0.4Sc-0.35Zr-0.9Mn-Si-0.6Ti-0.6Cu-0.25Cr (wt.%). The deposition process was carried out using an LDF3000-40 EHLD system (Laserline GmbH, Muelheim, Germany), which is composed of a high-speed lathe and laser and powder feeding system. The laser adopted in this paper is a LDF3000-40 semiconductor pulse laser (Laserline GmbH, Muelheim, Germany). The pulse duration and wavelength of the laser are 100 ms and

960~1060 $\pm$ 10 nm, respectively. During processing, the laser beam is focused by a focusing lens group. A detailed introduction to the EHLD system can be found in Ref. [1]. In this paper, the coating was prepared by depositing two AlMgMnSc alloy layers using the following processing parameters: a powder feed rate of 6 g/min, laser spot diameter of 1.2 mm, laser power of 1500 W, scanning speed of 5.5 m/min, and overlapping ratio of 50%. According to our previous work on the optimization of processing parameters, crack-free EHLDed AlMgMnSc alloy coatings with a metallurgical bond to the substrate can be obtained by using the above processing parameters. Before deposition, the surface of the 6061 aluminium-alloy axle was polished and cleaned with alcohol and acetone. During the deposition process, argon was adopted as a powder carrier gas and shielding gas. A schematic illustration of the EHLD process is shown in Figure 2.
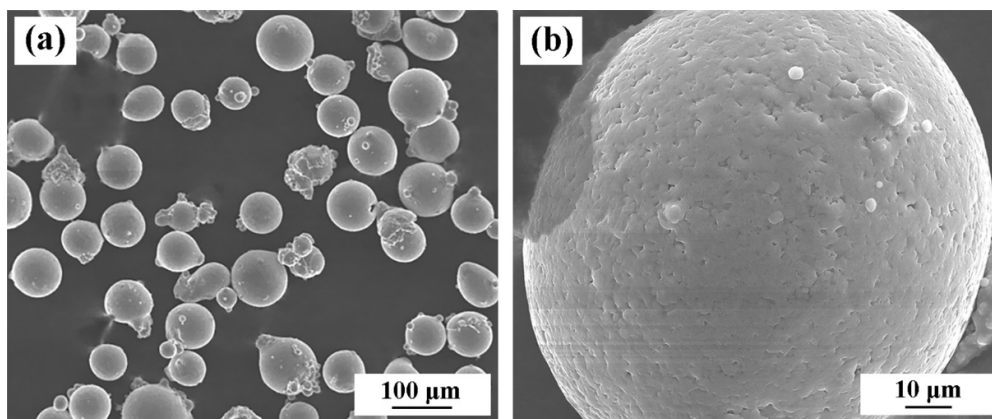
**Figure 1.** SEM images of raw powders. (**a**) Starting precursors. (**b**) Surface morphology of the powder.
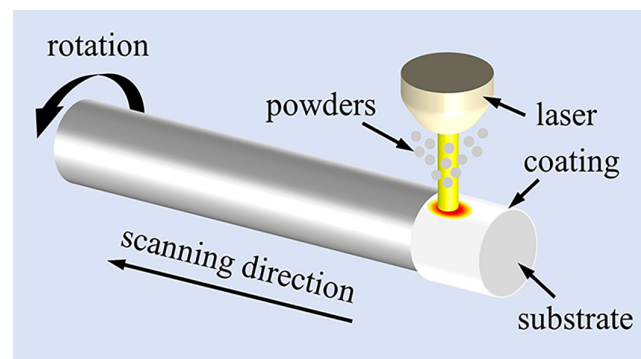
Figure 2. Schematic illustration of the EHLD process.

After deposition, the fabricated sample was sectioned into pieces using electrical discharge wire cutting to analyse the microstructure, composition variation, and microhardness distribution of the longitudinal section of the prepared coating. The samples were ground with SiC grit paper and then polished using the standard mechanical polishing method. Mechanical polishing was conducted by adopting a Tegramin-20 polishing machine (Struers, Copenhagen, Denmark), and the duration of mechanical polishing is about 1 min. After mechanical polishing, a VibroMet 2 vibratory polisher (BUEHLER, Lake Bluff, IL, USA) was adopted to polish the surfaces of the samples. During vibratory polishing, SiO_2 turbid liquid was utilised as a grinding polishing media and the polishing time was 4 h. Microstructure, crystallographic orientations, grain size distributions, and composition variation were determined by a JSM7900F scanning electron microscope (SEM) (JEOL, Tokyo, Japan) equipped with energy-dispersive X-ray analysis (EDX). Microhardness distributions along depth direction were tested by using an FM-800 Microhardness tester (Future-Tech, Tokyo, Japan), with 10 s loading time and under loads of 50 g. The average hardness of each position was calculated from three measurements.

3. Results and Discussion

To reveal the microstructure formation mechanism of the prepared AlMgMnSc alloy coating, the change of composition, grain morphology, grain size, and crystallographic orientation along the deposition direction are analysed. In addition, to verify the feasibility of repairing aluminium alloys by utilising the EHLD technique and AlMgMnSc alloy powders, the microhardness distribution along the depth direction is measured.

Variation in composition along the depth direction of the fabricated sample was measured by EDX, and the result is given in Figure 3. As is shown, with an increase in the distance away from the substrate, the contents of Fe and Zn decrease while the contents of Mg, Sc, Zr, Si, Mn, Ti and Cr are increased. The average compositions of layers 1 and 2 are Al-3.5Mg-0.36Sc-0.16Zr-Si-0.5Ti-0.22Cr-0.8Mn-0.17Fe-0.6Cu-0.2Zn (wt.%) and Al-4.4Mg-0.42Sc-0.32Zr-Si-0.55Ti-0.24Cr-0.9Mn-0.15Fe-0.6Cu-0.01Zn (wt.%), respectively. During deposition of layer 1, part of the substrate is melted and mixed with newly deposited AlMgMnSc alloy. Thus, a layer with a composition between 6061 aluminium alloy and AlMgMnSc alloy is established. As deposition continues, the composition of layer 2 is more close to the AlMgMnSc alloy. Finally, a coating with changed compositions is formed.
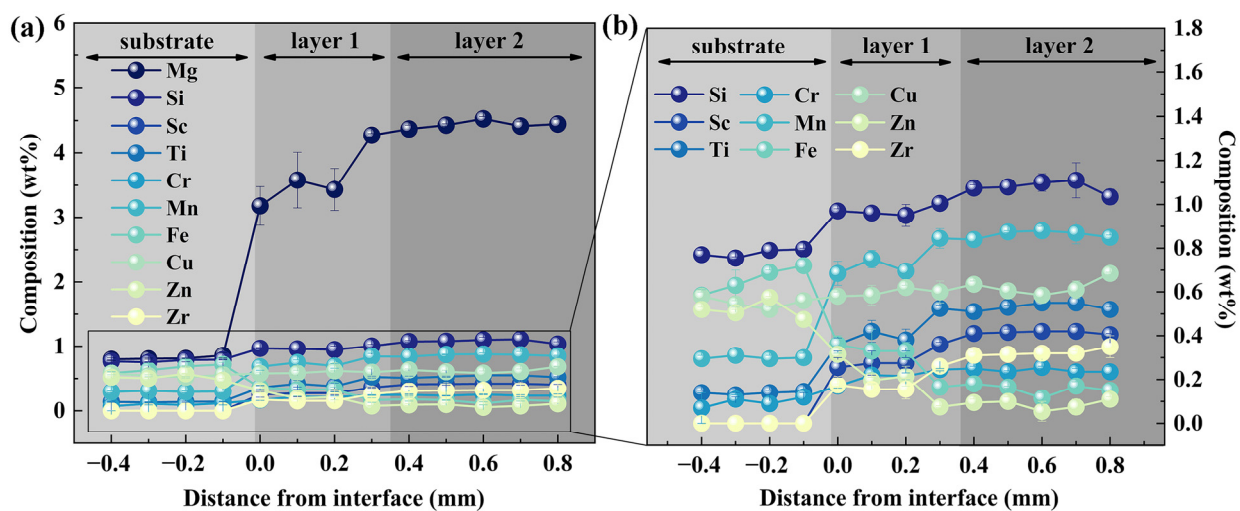

Figure 3. Variation of composition along the depth direction. (**a**) Change in composition. (**b**) Partial magnification of Figure 3a.

Figure 4 shows SEM images of a cross section of the fabricated sample. An overview of the coating in Figure 4a indicates that the coating is dense and crack-free. Also, pores with an average diameter smaller than 100 μm are observed. The boundary between the substrate and the coating is illustrated in Figure 4b, revealing that the interface between the coating and the substrate is smooth, continuous, and well-bonded. The microstructure of layers 1 and 2 in Figure 4c,d indicates that both layers are composed of precipitation phases and an α-Al matrix. The microstructure of layer 1 in Figure 4c reveals that most of the precipitation phases exhibit a lath-shaped morphology. Also, a small amount of nano-scaled precipitation phases with a dot-shaped morphology are visible. Meanwhile, the precipitation phases in layer 1 mainly precipitate around the grain boundaries of α-Al, displaying a lamellar structure. The microstructure of layer 2 in Figure 4d shows that nano-scaled precipitation phases with particle-like morphology disperse evenly through equiaxed α-Al grains.

To further analyse the microstructural characteristics of different layers, electron backscattered diffraction (EBSD) analysis is adopted. The EBSD results of layer 1 are shown in Figure 5. The orientation map in Figure 5a indicates that layer 1 has a unique heterogeneous grain structure, which can essentially be divided into three regimes based on the variation in grain size and morphology: (i) equiaxed grains at the bottoms of melting pools (EGB), (ii) columnar grains grown from the bottoms of melting pools (CGB), and

(iii) equiaxed grains at the tops of melting pools (EGT). The EGB mainly distributes at the melting boundary close to the previously deposited layer, while the CGB primarily distributes at the melting boundary adjacent to the substrate. In addition, columnar grains preferred to grow along the direction perpendicular to the melting boundary. From Figure 5b, it is noticed that the distribution of grain size in the EGB region is not uniform. In the colony of fine equiaxed grains (FEGB), there is a band of relatively coarse equiaxed grains (CEGB).
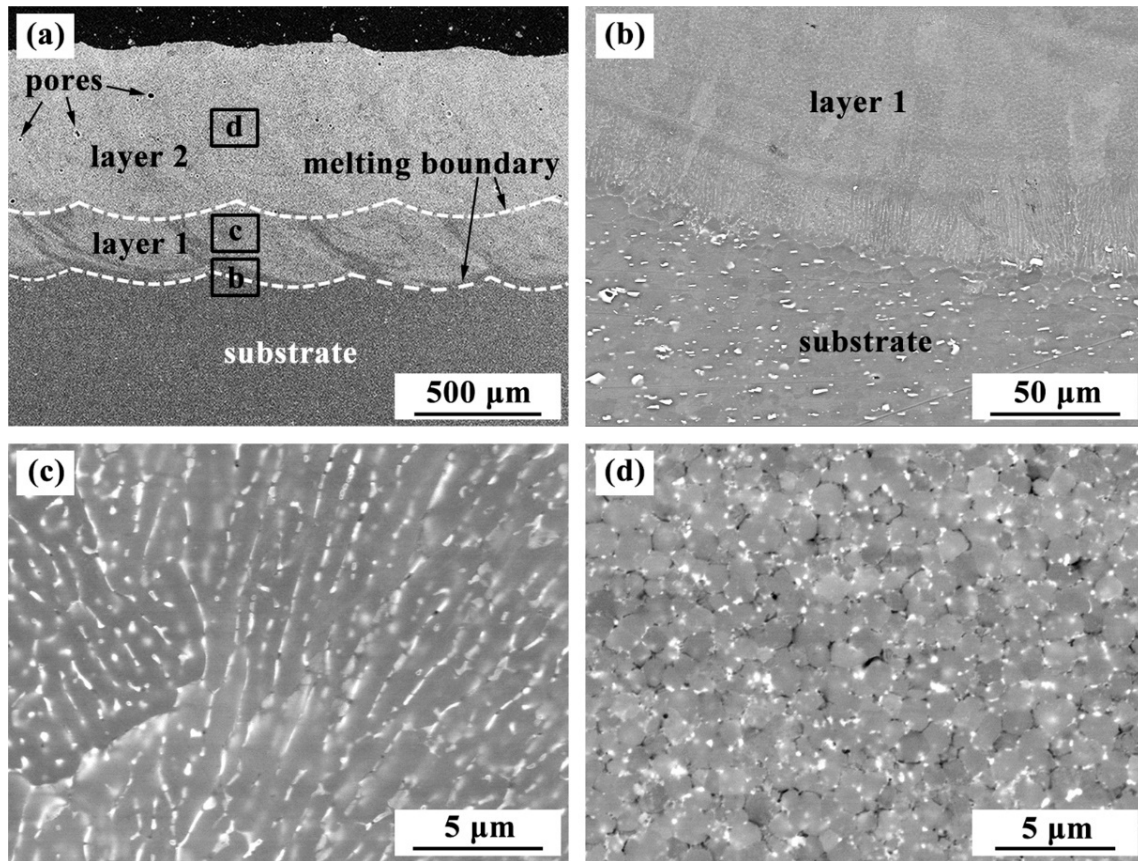

Figure 4. SEM images of a cross section of the fabricated sample. (**a**) Overview of the coating. (**b**) Boundary between the substrate and the coating. (**c**) Microstructure of layer 1. (**d**) Microstructure of layer 2.
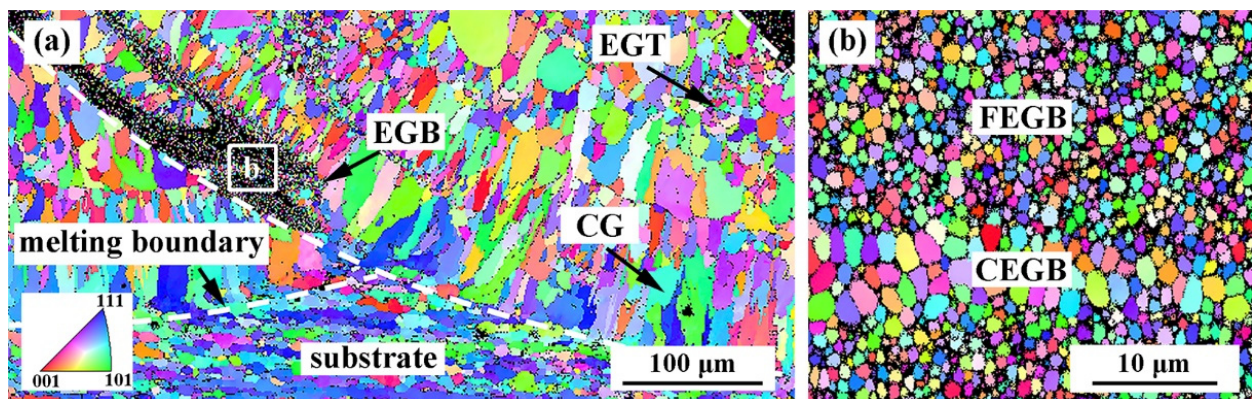
Figure 5. EBSD results of layer 1. (**a**) Orientation map of layer 1. (**b**) Orientation map of the EGB region.

To further analyse the difference between crystallographic orientations and the grain size of different regimes in layer 1, the texture index and grain size distributions are quantitatively compared in Figure 6. Pole figures (PFs) of the FEGB, CEGB, and EGT regions in Figure 6a–c illustrate that equiaxed grains in layer 1 are randomly oriented, which can be confirmed by the random colour in Figure 5. The maximal texture indices of the FEGB, CEGB, and EGT regions are 1.936, 4.314, and 5.774, respectively. The inverse pole figure (IPF) of the CG region in Figure 6d suggests that columnar grains mainly grow along the crystallographic direction of [212] and [103]. Grain-size data calculated based on the EBSD spectrum in Figure 6e–g show that the grain size distributions of the FEGB, CEGB, and EGT regions are 0.2~1.8 μm, 0.2~2.8 μm, and 1.7~41.9 μm, respectively. The average grain sizes of the equiaxed grains in the FEGB, CEGB, and EGT regions are about 1.0 μm, 1.9 μm, and 16.0 μm, respectively.
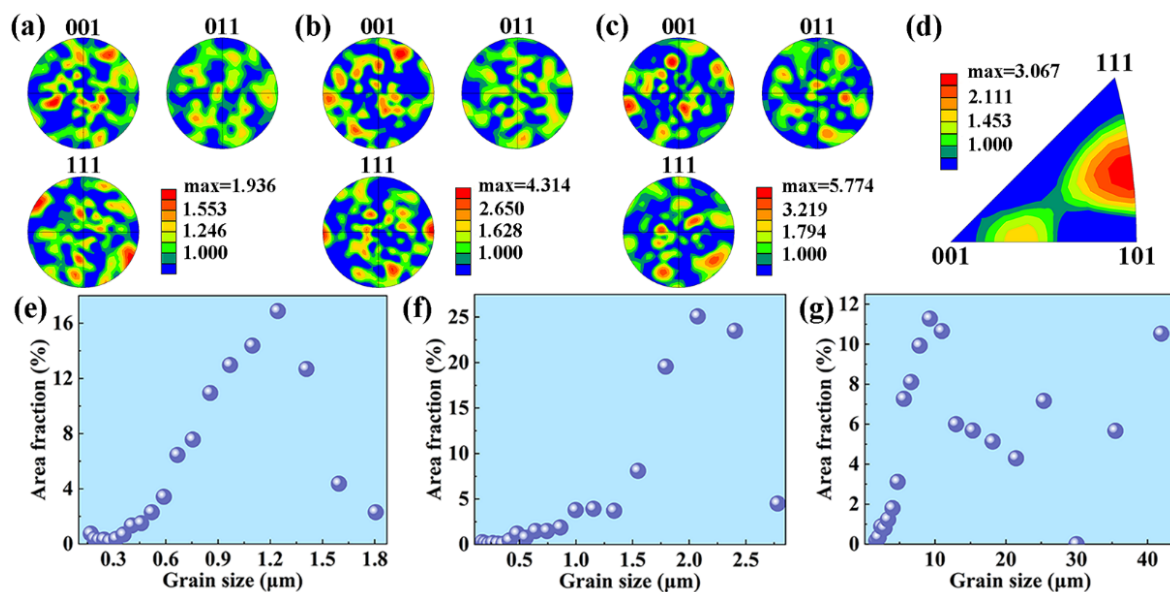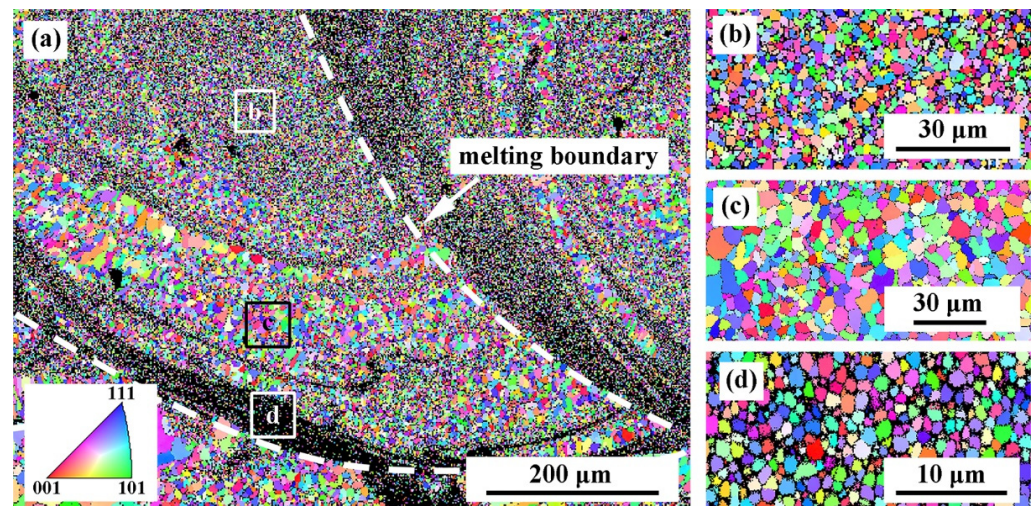

Figure 6. Crystallographic orientations and grain size distributions of different regimes in layer 1. (**a**) PF of the FEGB region. (**b**) PF of the CEGB region. (**c**) PF of the EGT region. (**d**) IPF of the CG region. (**e**) Grain size distribution of the FEGB region. (**f**) Grain size distribution of the CEGB region. (**g**) Grain size distribution of the EGT region.

The grain structure of the AMed AlMgMnSc aluminium alloy is primarily determined by the solidification condition of the melting pool and precipitation of primary $Al_3(Sc, Zr)$ particles [37]. During solidification, a high temperature gradient (G) at the solidification interface and low solidification velocity (V) favour the formation of columnar grains growing along the direction parallel to the direction of the maximum thermal gradient. By contrast, high V and low G promote the formation of equiaxed grains [38,39]. Additionally, primary $Al_3(Sc, Zr)$ particles tend to precipitate from liquid metals before the onset of α-Al solidification. The similar lattice constants of α-Al and $Al_3(Sc, Zr)$ make the $Al_3(Sc, Zr)$ particles effective nucleation cores for the following solidification of α-Al grains [37]. As a result, the formation of a fine equiaxed grain structure is strongly promoted.

During the deposition of layer 1, the G and cooling rate (R) of the melting pool are relatively large, due to the low temperature of substrate. Rapid cooling during solidification may suppress precipitation of primary $Al_3(Sc, Zr)$ particles [31]. Additionally, G usually enhances with the increase of depth in the melting pool, while V is the highest at the top of the melting pool [40,41]. Therefore, columnar grains prefer to form at the bottom of the melting pool, while equiaxed grains are obtained at the top of the melting pool [42]. Consequently, layer 1 mainly contains large columnar and equiaxed grains. The addition of Sc does not result in a widespread presence of fine equiaxed grains. In layer 1, it is also noticed that only a small amount of fine equiaxed grains are formed at the melting

boundary close to the previously deposited layer. The existence of fine equiaxed grains could be attributed to the high temperature of the previously prepared layer, which leads to a decrease in G and R. Under a relatively low R, primary Al_3(Sc, Zr) particles would be obtained in the melting pool, providing heterogeneous nucleation sites. Simultaneously, a low G promotes the formation of equiaxed grains. Generally, variation of local solidification conditions results in heterogeneity in the grain structure of layer 1.

EBSD results of layer 2 in Figure 7 show that the grain structure of layer 2 is quite different from that of layer 1, indicating that these two layers experience different modes of solidification. Orientation maps in Figure 7a–d reveal that no columnar grain is formed in layer 2, and most grains exist in the form of equiaxed grains. The fully equiaxed grain structure in layer 2 is similar to the AlMgSc aluminium alloys prepared using a laser-directed energy deposition technique [31,32]. Despite the similarity in grain morphology, the distribution of grain size in layer 2 is not uniform. According to the variation in grain size, layer 2 can be divided into three regimes: (i) fine equiaxed grains at the bottoms of melting pools (FEG), (ii) equiaxed grains with medium size at the centres of melting pools (MEG), and (iii) coarse equiaxed grains at tops of melting pools (CEG).


Figure 7. EBSD results of layer 2. (**a**) Orientation map of layer 2. (**b**) Orientation map of the MEG region. (**c**) Orientation map of the CEG region. (**d**) Orientation map of the FEG region.

To study the differences in crystallographic orientations and grain size of different regimes in layer 2, the texture index and grain size distributions are quantitatively investigated in Figure 8. PFs of the FEG, MEG, and CEG regions in Figure 8a–c show that layer 2 presents strong anisotropy, and grains in layer 2 have no obvious preferred orientation. The maximal texture indices of the FEG, MEG, and CEG regions are 2.054, 1.465, and 2.149, respectively. Grain-size data obtained from the EBSD spectrum in Figure 8d–f show that the grain size distributions in the FEG, MEG, and CEG regions are determined to be 0.2~1.8 μm, 0.7~5.0 μm, and 0.7~12.1 μm, respectively. The average grain sizes of the equiaxed grains in the FEG, MEG, and CEG regions are about 1.2 μm, 2.2 μm, and 5.6 μm, respectively. Layer 2 displays an average grain size of about 4.5 μm. Compared with layer 1, it is clear that the distribution of grain size in layer 2 is more uniform. According to previous research, a fully equiaxed grain structure with grain sizes of 2–30 μm could be obtained by using laser-directed energy deposition [32]. As can be seen, the alloy prepared through the EHLD in this work is smaller than the laser-directed energy-deposited alloy.

During the deposition of layer 2, G and R are relatively small due to the high temperature of layer 1. Compared with layer 1, precipitation of primary Al_3(Sc, Zr) particles is more homogeneous in the entire melting pool. The enrichment of primary Al_3(Sc, Zr) particles leads to the formation of a fully equiaxed grain structure. The formation process of fine equiaxed grains is illustrated in Figure 9. In addition, Figure 7 indicates that the

distribution of grain size in layer 2 is not uniform. This may be ascribed to the convection of liquid in the melting pool [43]. It is speculated that liquid flow leads to a non-uniform distribution of primary Al$_3$(Sc, Zr) particles, resulting in the variation in grain size.
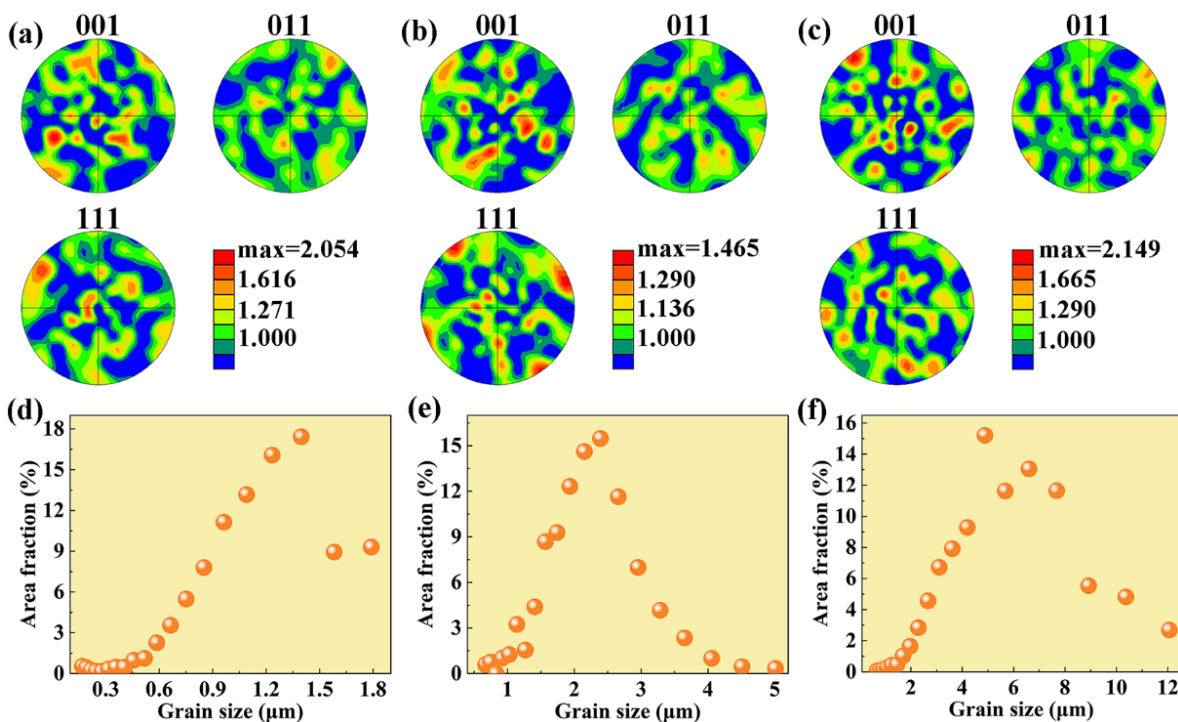

Figure 8. Crystallographic orientations and grain size distributions of different regimes in layer 2. (**a**) PF of the FEG region. (**b**) PF of the MEG region. (**c**) PF of the CEG region. (**d**) Grain size distribution of the FEG region. (**e**) Grain size distribution of the MEG region. (**f**) Grain size distribution of the CEG region.
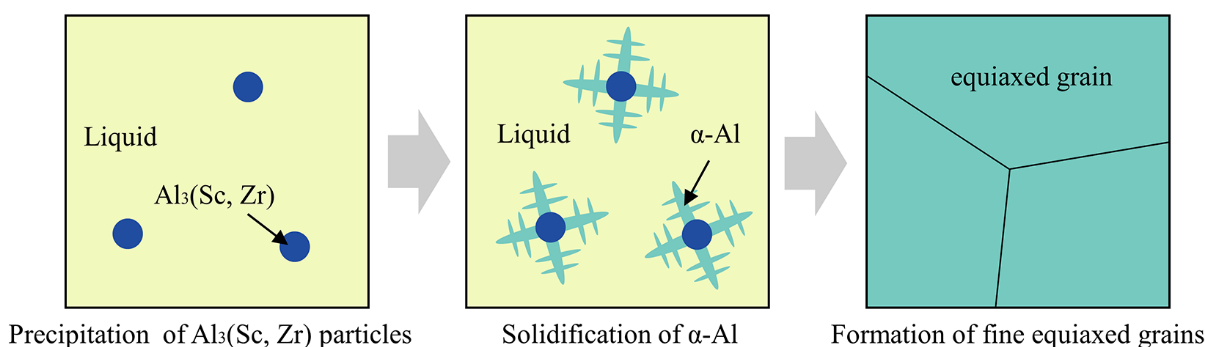
Figure 9. Formation process of fine equiaxed grains.

As is reported by previous works, Sc-containing aluminium alloy fabricated by selective laser melting normally presents a bimodal grain structure. That is, a band of equiaxed grains with no preferential crystallographic orientation forms at the melting boundary, while columnar grains growing along the deposition direction dominate the centre of the melting pool [44,45]. On the other hand, a fully equiaxed fine grain structure can be obtained in Sc-containing aluminium alloy prepared through laser-directed energy deposition, due to a relatively low cooling rate and temperature during deposition [32]. As for the prepared coating in this paper, the unique fabrication process of the EHLD leads to different microstructure features. The variation in solidification conditions results in a changed grain morphology along the building direction. That is, layer 1 displays a heterogeneous grain structure, while layer 2 consists of a fully equiaxed grain structure.

Figure 10 presents variations in microhardness along the depth direction of the fabricated sample and micrographs of microhardness indent marks. As can be seen, the microhardness of layers 1 (about 104~112 HV) and 2 (about 107~118 HV) are similar to the substrate (about 105 HV). Hence, it could be suggested that using AlMgMnSc alloy powders as raw materials to repair the surfaces of traditional high-strength aluminium-alloy components via the EHLD technique is applicable. It is also noticed that microhardness fluctuates obviously within the deposited layers. As illustrated in Figures 5 and 7, the fabricated coating presents a mixed microstructure. That is, there is a change in grain morphology and grain size along the deposition direction. Therefore, it is speculated that the fluctuation in microhardness may be ascribed to the uneven distribution of the microstructure.
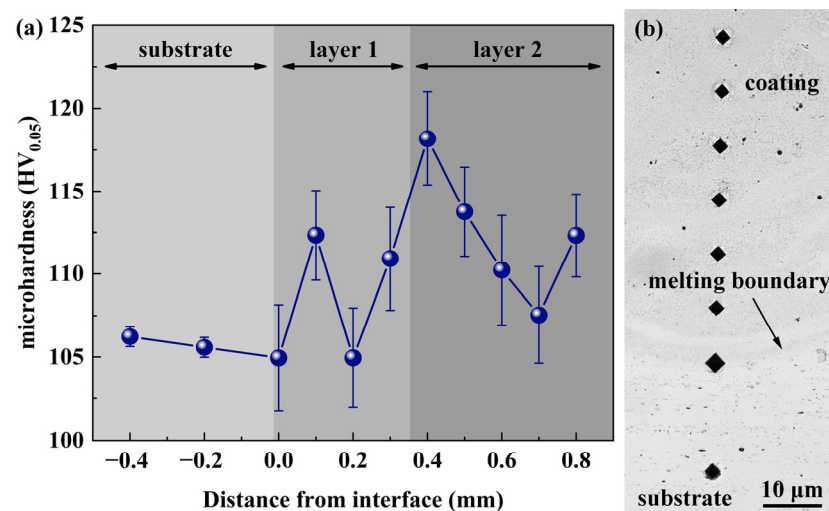
Figure 10. Variation of microhardness along the depth direction. (**a**) Microhardness values. (**b**) Micrographs of microhardness indent marks.

To sum up, this paper reveals the microstructure and microhardness of the EHLDed AlMgMnSc alloy coating for the first time. It is found that a change in the solidification conditions within the melting pool results in the variation in grain morphology along the deposition direction. Moreover, fully equiaxed fine grains can be obtained with an increase in the deposition layer. In addition, the fabricated coating exhibits a similar microhardness to the 6061 aluminium-alloy substrate. This paper offers a deep insight into the microstructure and mechanical performance of the EHLDed AlMgMnSc alloy coating.

4. Conclusions

In this paper, an AlMgMnSc high-strength aluminium-alloy coating was prepared on a 6061 aluminium-alloy axle using the EHLD technique. The grain structure, composition distribution, and microhardness variation of the fabricated coating were studied.

The results reveal that the prepared coating is dense and crack free and is well-bonded with the substrate. Additionally, with an increase in distance away from the substrate, there is a change in chemical compositions along the deposition direction. Moreover, due to the variation of local solidification conditions, layer 1 mainly contains large columnar and equiaxed grains. Only a small amount of fine equiaxed grains are formed at the melting boundary. The average grain size of the equiaxed grains in the FEGB, CEGB, and EGT regions in layer 1 are about 1.0 μm, 1.9 μm, and 16.0 μm, respectively. Meanwhile, layer 2 consists of a fully equiaxed grain structure with no preferential crystallographic orientation. The distribution of grain size in layer 2 is not uniform. The average grain sizes of the equiaxed grains in the FEG, MEG, and CEG regions in layer 2 are about 1.2 μm, 2.2 μm, and 5.6 μm, respectively. Furthermore, the microhardness of the coating (about 104~118 HV) is similar to the substrate (about 105 HV), proving the feasibility of repairing the surfaces of traditional high-strength aluminium-alloy components using AlMgMnSc alloy

powders through the EHLD technique. Compared with conventional laser deposition, the EHLD technique presents higher depositing efficiency. In the meantime, primary $Al_3(Sc, Zr)$ particles in AlMgMnSc alloy promote the formation of equiaxed fine grains, inhibiting the generation of solidification cracking remarkably. Also, the addition of Sc significantly improves the mechanical properties of the alloy. By combining the advantages of the EHLD technique and an AlMgMnSc alloy, this paper provides a new approach to rapidly modify the surfaces of aluminium-alloy components with high performance.

Author Contributions: Conceptualization, Y.W.; methodology, P.X. and B.D.; investigation, Y.W., P.X. and P.T.; resources, Y.W. and B.D.; writing—original draft, Y.W.; writing—review and editing, B.C., P.T. and C.H.; visualization, C.H.; funding acquisition, Y.W.; supervision, B.C.; project administration, Y.W. All authors have read and agreed to the published version of the manuscript.

Data Availability Statement: The data presented in this study are available on request from the corresponding author.

Conflicts of Interest: The authors declare no conflicts of interest. Author Yu Wu and Bingqing Chen are employed by 3D Printing Research & Engineering Technology Center, Beijing Institute of Aeronautical Materials. Author Peixin Xu and Borui Du are employed by China Machinery Institute of Advanced Materials (Zhengzhou) Co,. Ltd. Author Pengjun Tang is employed by Institute of Aluminium Alloy, Beijing Institute of Aeronautical Materials. Author Chen Huang is employed by the Petrochemical Department, China National Petroleum & Chemical Planning Institute. All authors declare that the research was conducted in the absence of any commercial or financial relationships that could be construed as a potential conflict of interest.

References

1. Yuan, W.; Li, R.; Chen, Z.; Gu, J.; Tian, Y. A comparative study on microstructure and properties of traditional laser cladding and high-speed laser cladding of Ni45 alloy coatings. *Surf. Coat. Technol.* **2021**, *405*, 126582. [CrossRef]
2. Ren, Y.; Li, L.; Zhou, Y.; Wang, S. In situ synthesized VC reinforced Fe-based coating by using extreme high-speed laser cladding. *Mater. Lett.* **2022**, *315*, 131962. [CrossRef]
3. Zhang, Q.; Li, M.; Wang, Q.; Qi, F.; Kong, M.; Han, B. Investigation of the microstructure and properties of CoCrFeNiMo high-entropy alloy coating prepared through high-speed laser cladding. *Coatings* **2023**, *13*, 1211. [CrossRef]
4. Zhang, W.; Liu, Y.; Hu, D.; Lv, H.; Yang, Q. Experimental and numerical simulation studies of the flow characteristics and temperature field of Fe-based powders in extreme high-speed laser cladding. *Opt. Laser Technol.* **2024**, *170*, 110317. [CrossRef]
5. Lampa, C.; Smirnov, I. High speed laser cladding of an iron based alloy developed for hard chrome replacement. *J. Laser Appl.* **2019**, *31*, 022511. [CrossRef]
6. Liang, Y.; Liao, Z.Y.; Zhang, L.L.; Cai, M.W.; Wei, X.S.; Shen, J. A review on coatings deposited by extreme high-speed laser cladding: Processes, materials, and properties. *J. Laser Appl.* **2023**, *164*, 109472. [CrossRef]
7. Koß, S.; Vogt, S.; Göbel, M.; Schleifenbaum, J.H. Coating of aluminum with high deposition rates through extreme high-speed laser application. *J. Therm. Spray Technol.* **2023**, *32*, 1689–1697. [CrossRef]
8. Xiao, M.; Gao, H.; Sun, L.; Wang, Z.; Jiang, G.; Zhao, Q.; Guo, C.; Li, L.; Jiang, F. Microstructure and mechanical properties of Fe-based amorphous alloy coatings prepared by ultra-high speed laser cladding. *Mater. Lett.* **2021**, *297*, 130002. [CrossRef]
9. Chen, S.; Liu, Z.; Ning, H.; Liu, F. Study on high-temperature oxidation and hot corrosion characteristics of Cr60Ni40 laser cladding layer. *Mater. Lett.* **2023**, *342*, 134352. [CrossRef]
10. Osama, A.; Luo, L.Y.; Muhammad, Y.; Li, C.J.; Li, C.X. Enhanced tribological properties of LA43M magnesium alloy by Ni60 coating via ultra-high-speed laser cladding. *Coatings* **2020**, *10*, 638.
11. Xu, X.; Lu, H.; Qiu, J.; Luo, K.; Su, Y.; Xing, F.; Lu, J. High-speed-rate direct energy deposition of Fe-based stainless steel: Process optimization, microstructural features, corrosion and wear resistance. *J. Manuf. Process.* **2022**, *75*, 243–258. [CrossRef]
12. Xu, X.; Du, J.L.; Luo, K.Y.; Peng, M.X.; Xing, F.; Wu, L.J.; Lu, J.Z. Microstructural features and corrosion behavior of Fe-based coatings prepared by an integrated process of extreme high-speed laser additive manufacturing. *Surf. Coat. Technol.* **2021**, *422*, 127500. [CrossRef]
13. Yuan, W.; Li, R.; Zhu, Y.; Zhao, Y.; Zhang, X.; Liu, B.; Zhang, B. Structure and properties of nickel-plated CNTs/Fe-based amorphous composite coatings fabricated by high-speed laser cladding. *Surf. Coat. Technol.* **2022**, *438*, 128363. [CrossRef]
14. Li, R.; Yuan, W.; Yue, H.; Zhu, Y. Study on microstructure and properties of Fe-based amorphous composite coating by high-speed laser cladding. *Opt. Laser Technol.* **2022**, *146*, 107574. [CrossRef]
15. Wu, Z.; Qian, M.; Brandt, M.; Matthews, N. Ultra-high-speed laser cladding of Stellite® 6 alloy on mild steel. *JOM* **2020**, *72*, 4632–4638. [CrossRef]

16. Schopphoven, T.; Gasser, A.; Wissenbach, K.; Poprawe, R. Investigations on ultra-high-speed laser material deposition as alternative for hard chrome plating and thermal spraying. *J. Laser Appl.* **2016**, *28*, 022501. [CrossRef]
17. Montero-Sistiaga, M.L.; Mertens, R.; Vrancken, B.; Wang, X.; Van Hooreweder, B.; Kruth, J.P.; Van Humbeeck, J. Changing the alloy composition of Al7075 for better processability by selective laser melting. *J. Mater. Process. Technol.* **2016**, *238*, 437–445. [CrossRef]
18. Braga, D.F.O.; Tavares, S.M.O.; da Silva, L.F.M.; Moreira, P.M.G.P.; de Castro, P.M.S.T. Advanced design for lightweight structures: Review and prospects. *Prog. Aerosp. Sci.* **2014**, *69*, 29–39. [CrossRef]
19. Arbo, S.M.; Tjøtta, S.; Boge, M.H.; Tundal, U.; Li, J.; Dumoulin, S.; Jensrud, O. The potential of cast stock for the forging of aluminum components within the automotive industry. *Metals* **2024**, *14*, 90. [CrossRef]
20. Li, S.S.; Yue, X.; Li, Q.Y.; Peng, H.L.; Dong, B.X.; Liu, T.S.; Yang, H.Y.; Fan, J.; Shu, S.L.; Qiu, F.; et al. Development and applications of aluminum alloys for aerospace industry. *J. Mater. Res. Technol.* **2023**, *27*, 944–983. [CrossRef]
21. Fan, X.; Yuan, S. Innovation for forming aluminum alloy thin shells at ultra-low temperature by the dual enhancement effect. *Int. J. Extrem. Manuf.* **2022**, *4*, 0330011.
22. Ogunsemi, B.T.; Abioye, T.E.; Ogedengbe, T.I.; Zuhailawati, H. A review of various improvement strategies for joint quality of AA 6061-T6 friction stir weldments. *J. Mater. Res. Technol.* **2021**, *11*, 1061–1089. [CrossRef]
23. Chandla, N.K.; Kant, S.; Goud, M.M. Mechanical, tribological and microstructural characterization of stir cast Al-6061 metal/matrix composites—A comprehensive review. *Sādhanā* **2021**, *46*, 47. [CrossRef]
24. Bayoumy, D.; Schliephake, D.; Dietrich, S.; Wu, X.H.; Zhu, Y.M.; Huang, A.J. Intensive processing optimization for achieving strong and ductile Al-Mn-Mg-Sc-Zr alloy produced by selective laser melting. *Mater. Des.* **2021**, *198*, 109317. [CrossRef]
25. Tan, Q.; Liu, Y.; Fan, Z.; Zhang, J.; Yin, Y.; Zhang, M.X. Effect of processing parameters on the densification of an additively manufactured 2024 Al alloy. *J. Mater. Sci. Technol.* **2020**, *58*, 34–45. [CrossRef]
26. Stopyra, W.; Gruber, K.; Smolina, I.; Kurzynowski, T.; Kuźnicka, B. Laser powder bed fusion of AA7075 alloy: Influence of process parameters on porosity and hot cracking. *Addit. Manuf.* **2020**, *35*, 101270. [CrossRef]
27. Larini, F.; Casati, R.; Marola, S.; Vedani, M. Microstructural evolution of a high-strength Zr-Ti-Modified 2139 aluminum alloy for laser powder bed fusion. *Metals* **2023**, *13*, 924. [CrossRef]
28. Yao, S.; Wang, J.; Li, M.; Chen, Z.; Lu, B.; Shen, S.; Li, Y. LPBF-formed 2024Al alloys: Process, microstructure, properties, and thermal cracking behavior. *Metals* **2023**, *13*, 268. [CrossRef]
29. Xiao, X.; Guo, Y.; Zhang, R.; Bayoumy, D.; Shen, H.; Li, J.; Gan, K.; Zhang, K.; Zhu, Y.; Huang, A. Achieving uniform plasticity in a high strength Al-Mn-Sc based alloy through laser-directed energy deposition. *Addit. Manuf.* **2022**, *60*, 103273. [CrossRef]
30. Yang, K.V.; Shi, Y.; Palm, F.; Wu, X.; Rometsch, P. Columnar to equiaxed transition in Al-Mg(-Sc)-Zr alloys produced by selective laser melting. *Scr. Mater.* **2018**, *145*, 113–117. [CrossRef]
31. Wang, Z.; Lin, X.; Kang, N.; Chen, J.; Tang, Y.; Tan, H.; Yu, X.; Yang, H.; Huang, W. Directed energy deposition additive manufacturing of a Sc/Zr-modified Al–Mg alloy: Effect of thermal history on microstructural evolution and mechanical properties. *Mat. Sci. Eng. A* **2021**, *802*, 140606. [CrossRef]
32. Hua, Q.; Wang, W.; Li, R.; Zhu, H.; Lin, Z.; Xu, R.; Yuan, T.; Liu, K. Microstructures and mechanical properties of Al-Mg-Sc-Zr alloy additively manufactured by laser direct energy deposition. *Chin. J. Mech. Eng. Addit. Manuf. Front.* **2022**, *1*, 100057. [CrossRef]
33. Shi, Y.; Rometsch, P.; Yang, K.; Palm, F.; Wu, X. Characterisation of a novel Sc and Zr modified Al–Mg alloy fabricated by selective laser melting. *Mater. Lett.* **2017**, *196*, 347–350. [CrossRef]
34. Spierings, A.B.; Dawson, K.; Kern, K.; Palm, F.; Wegener, K. SLM-processed Sc- and Zr- modified Al-Mg alloy: Mechanical properties and microstructural effects of heat treatment. *Mat. Sci. Eng. A* **2017**, *701*, 264–273. [CrossRef]
35. Spierings, A.B.; Dawson, K.; Heeling, T.; Uggowitzer, P.J.; Schäublin, R.; Palm, F.; Wegener, K. Microstructural features of Sc- and Zr-modified Al-Mg alloys processed by selective laser melting. *Mater. Des.* **2017**, *115*, 52–63. [CrossRef]
36. Shi, Y.; Yang, K.; Kairy, S.K.; Palm, F.; Wu, X.; Rometsch, P.A. Effect of platform temperature on the porosity, microstructure and mechanical properties of an Al–Mg–Sc–Zr alloy fabricated by selective laser melting. *Mat. Sci. Eng. A* **2018**, *732*, 41–52. [CrossRef]
37. Bayoumy, D.; Kan, W.; Wu, X.; Zhu, Y.; Huang, A. The latest development of Sc-strengthened aluminum alloys by laser powder bed fusion. *J. Mater. Sci. Technol.* **2023**, *149*, 1–17. [CrossRef]
38. Wang, T.; Zhu, Y.Y.; Zhang, S.Q.; Tang, H.B.; Wang, H.M. Grain morphology evolution behavior of titanium alloy components during laser melting deposition additive manufacturing. *J. Alloy Compd.* **2015**, *632*, 505–513. [CrossRef]
39. Zhu, Y.-Y.; Tang, H.-B.; Li, Z.; Cheng, X.; He, B. Solidification behavior and grain morphology of laser additive manufacturing titanium alloys. *J. Alloy Compd.* **2019**, *777*, 712–716. [CrossRef]
40. Liang, Y.-J.; Cheng, X.; Wang, H.-M. A new microsegregation model for rapid solidification multicomponent alloys and its application to single-crystal nickel-base superalloys of laser rapid directional solidification. *Acta Mater.* **2016**, *118*, 17–27. [CrossRef]
41. Wang, J.; Wang, H.; Cheng, X.; Zhang, B.; Wu, Y.; Zhang, S.; Tian, X. Prediction of solidification microstructure of titanium aluminum intermetallic alloy by laser surface remelting. *Opt. Laser Technol.* **2022**, *147*, 107606. [CrossRef]
42. Hunt, J.D. Steady state columnar and equiaxed growth of dendrites and eutectic. *Mater. Sci. Eng. A* **1984**, *65*, 75–83. [CrossRef]
43. Qian, T.-T.; Liu, D.; Tian, X.-J.; Liu, C.-M.; Wang, H.-M. Microstructure of TA2/TA15 graded structural material by laser additive manufacturing process. *Trans. Nonferrous Met. Soc.* **2014**, *24*, 2729–2736. [CrossRef]

44.   Jia, Q.; Rometsch, P.; Kürnsteiner, P.; Chao, Q.; Huang, A.; Weyland, M.; Bourgeois, L.; Wu, X. Selective laser melting of a high strength Al-Mn-Sc alloy: Alloy design and strengthening mechanisms. *Acta Mater.* **2019**, *171*, 108–118. [CrossRef]
45.   Jia, Q.; Rometsch, P.; Cao, S.; Zhang, K.; Wu, X. Towards a high strength aluminium alloy development methodology for selective laser melting. *Mater. Des.* **2019**, *174*, 107775. [CrossRef]